Research Square

Preprints are preliminary reports that have not undergone peer review.
They should not be considered conclusive, used to inform clinical practice,
or referenced by the media as validated information.

Bifidobacterium longum Bianquejun 19 Suppresses Helicobacter pylori Motility and Colonization by Disrupting Energy Metabolism

Yajie Zhang
Beijing University of Agriculture
Lijuan Kang
HeBei Yuzhilin Pharmaceutical Co.Ltd
Yinqing Li
Hebei Technology Innovation Center of Precise nutrition and health
Liang Zhao
China Agricultural University
Yuanhong Xie
Beijing University of Agriculture
Hongxin Zhang
Beijing University of Agriculture
Ran Wang
China Agricultural University
Junhua Jin
jinjunhua002008@163.com

Beijing University of Agriculture

Research Article

Keywords: Bifidobacterium longum Bianquejun 19, Helicobacter pylori, energy metabolism, flagellar motility, gastric mucosal injury, colonization-related functions

Posted Date: October 5th, 2026

DOI: https://doi.org/10.21203/rs.3.rs-11058208/v1

License: This work is licensed under a Creative Commons Attribution 4.0 International License.
Read Full License

Additional Declarations: No competing interests reported.

Bifidobacterium longum Bianquejun 19 Suppresses *Helicobacter pylori* Motility and Colonization by Disrupting Energy Metabolism

Yajie Zhang[a], Lijuan Kang[b], Yinqing Li[c], Liang Zhao[d e], Yuanhong Xie[a], Hongxing Zhang[a], Ran Wang[f *], Junhua Jin[a *]

a Beijing laboratory of Food Quality and Safety, College of Food Science and Engineering, Beijing University of Agriculture, Beijing 102206, China;

b HeBei Yuzhilin Pharmaceutical Co.Ltd, Hebei, 050000, China;

c Hebei Technology Innovation Center of Precise nutrition and health, Hebei, 050000, China;

d College of Food Science and Nutritional Engineering, China Agricultural University, Beijing 100083, China;

e Research Center for Probiotics, China Agricultural University, Sanhe 065200, China;

f Key Laboratory of Functional Dairy, Department of Nutrition and Health, China Agricultural University, Beijing 100193, China;

* Corresponding author.

Email address: 19313960071@163.com (Y. Zhang), kangijuan1006@163.com (L. Kang), liagh@126.com (Y. Li), lzhao@cau.edu.cn (L. Zhao), xieyuanh@163.com (Y.Xie), hxzhang511@163.com (H.Zhang), wangran@cau.edu.cn (R. Wang), jinjunhua002008@163.com (J. Jin).

Abstract

The mechanisms by which probiotics interfere with *Helicobacter pylori* remain incompletely understood. This study systematically evaluated the effects of *Bifidobacterium longum* Bianquejun 19 on *H. pylori*-related biological phenotypes and validated these effects using metatranscriptomic analysis, in vitro physiological measurements, and animal experiments. *B. longum* Bianquejun 19 inhibited the growth of *H. pylori*. Its fermentation supernatant exhibited strong antibacterial activity both before and after pH neutralization, producing inhibition zones of 19.00–24.00 mm. In the competition model, the bacterial suspension reduced *H. pylori* adhesion and invasion by up to 71.41% and 73.57% in the competition model, respectively. Metatranscriptomic analysis showed that nine genes associated with central carbon metabolism were downregulated by 1.68–2.49-fold, while 15 genes involved in the respiratory chain were downregulated by 2.00–5.30-fold. Among these, the ATP synthase-related genes atpE and atpD were downregulated by 2.18- and 1.48-fold, respectively. Acetyl-CoA levels initially increased and subsequently decreased, ATP levels declined from 783.33 nmol/10^4 bacteria at 0 h to 26.22 nmol/10^4 bacteria at 24 h, and $NADH/NAD^+$ homeostasis was disrupted. The key flagellar genes fliN and fliI were downregulated by 1.53- and 1.74-fold, respectively, while the virulence-associated gene cagA was downregulated by 2.14-fold. The motility of *H. pylori* was markedly impaired: the radius of the motility zone decreased significantly from 11.6 mm to 4.6 mm after 4 h, and no obvious motility zone was observed after 8 h. These changes were accompanied by bacterial deformation and reduced or disrupted flagella. In the mouse infection model, all *B. longum* Bianquejun 19 intervention groups showed reduced inflammatory infiltration in the gastric mucosa and decreased gastric collagen deposition. Gastric CagA protein levels were significantly reduced in both the

bacterial suspension and fermentation supernatant groups. In addition, the colonic short-chain fatty acid profile showed component-dependent improvement. These findings indicate that *B. longum* Bianquejun 19 disrupts bacterial energy metabolism and motility-dependent colonization while modulating host inflammatory and metabolic responses, thereby alleviating *H. pylori*-induced collagen deposition in the gastric mucosa.

Keywords: *Bifidobacterium longum* Bianquejun 19; *Helicobacter pylori*; energy metabolism; flagellar motility; gastric mucosal injury; colonization-related functions

1 Introduction

Helicobacter pylori (*H. pylori*) is a pathogenic bacterium capable of long-term colonization in the gastric mucosa and is closely associated with the occurrence and progression of chronic gastritis, peptic ulcer, gastric mucosal atrophy, and gastric cancer[1]. Following infection, *H. pylori* can continuously induce neutrophil infiltration, chronic inflammatory responses, and mucosal injury, thereby promoting the progression of gastric tissue from inflammatory damage to structural remodeling and fibrosis[2].

The persistent pathogenicity of *H. pylori* depends not only on its colonization ability but also on host signaling disruption mediated by virulence factors such as CagA and VacA[3-5]. This bacterium can neutralize the local acidic environment through urease activity and penetrate the gastric mucus layer via flagellar motility, allowing it to adhere to gastric epithelial cells and maintain long-term infection under gastric acid stress, mucus barrier protection, and host immune pressure[1][6]. Flagellar motility plays a critical role in the initial colonization of *H. pylori*, its migration to suitable gastric mucosal niches, and the maintenance of persistent infection; impaired motility typically markedly attenuates its gastric colonization capacity[7]. Chen et al.

63 biochemically characterized the respiratory chain of *H. pylori* and identified NADPH as a major
64 respiratory electron donor, together with an electron-transfer pathway involving succinate
65 dehydrogenase and complexes II and III[8]. Marais et al. further showed, based on genomic and
66 biochemical evidence, that the specialized oxidative, fermentative, and respiratory pathways of *H.*
67 *pylori* are closely associated with its adaptation to the gastric environment and colonization-
68 related functions, including motility and adhesion[9]. These findings suggest that disrupting
69 respiratory electron transport and energy metabolism may weaken the metabolic adaptability and
70 colonization capacity of *H. pylori* [8][9].

71 At present, clinical eradication of *H. pylori* still mainly relies on antibiotic-based combination
72 therapy. However, the increasing antibiotic resistance rate and the disturbance of gastrointestinal
73 microbiota caused by antimicrobial treatment have become important factors limiting therapeutic
74 efficacy[10]. Therefore, the development of novel biological intervention strategies that can
75 interfere with pathogen colonization, attenuate virulence expression, and improve the host
76 microenvironment is of great significance[11]. In recent years, probiotics have attracted increasing
77 attention as potential adjunctive interventions. They can inhibit *H. pylori* growth by secreting
78 organic acids, bacteriocin-like substances[12-14], and other active metabolites, and can also weaken
79 its colonization and pathogenicity by competing for adhesion sites, enhancing the mucosal barrier,
80 and regulating immune responses[12][15].

81 However, most current studies have focused primarily on the clinical efficacy of probiotics as
82 adjuncts to eradication therapy, while the molecular responses of *H. pylori* to probiotic
83 intervention remain poorly understood. In particular, it remains unclear whether probiotics and
84 their soluble metabolites induce coordinated transcriptional changes in pathways associated with

central carbon metabolism, respiratory electron transport, redox homeostasis, and flagellar motility.

Based on this, the present study used the probiotic strain Bianquejun No. 19 as the research object to systematically evaluate its effects on *H. pylori* growth, adhesion, invasion, energy metabolism, and flagellar motility, and further investigated its intervention effects on gastric mucosal inflammatory responses and fibrotic injury in an animal infection model. By integrating in vitro antibacterial assays, cell adhesion and invasion assays, metatranscriptomic analysis, detection of key energy metabolites, motility assessment, transmission electron microscopy observation, and animal pathological examination, this study aims to clarify whether Bianquejun No. 19 can disrupt the central carbon metabolism, oxidative phosphorylation, and redox homeostasis of *H. pylori*, reduce ATP supply, and impair flagella-related motility, thereby weakening its colonization and pathogenic potential. This study also provides experimental evidence for probiotic-assisted intervention against *H. pylori* infection and gastric mucosal injury repair. From the perspective of practical application, Bianquejun No. 19 is expected to serve as an adjunctive probiotic strain for standard eradication therapy, helping reduce pathogen colonization burden, improve the gastric mucosal injury microenvironment, and provide a new microbiota-based intervention strategy for mucosal repair and recurrence risk control after eradication therapy.

2 Materials and Methods

2.1 Strains and Cells

The probiotic strain used in this study was *Bifidobacterium longum* Bianquejun 19 (preservation number: CGMCC.34431). After activation and culture, the bacterial suspension,

fermentation supernatant, and lysate supernatant were separately prepared to evaluate their effects on *H. pylori* growth, adhesion, and invasion, energy metabolism, and motility-dependent colonization. The *H. pylori* strain used in this study was the standard strain *H. pylori* 43504, provided by Hangzhou Bosai Biotechnology Co., Ltd. After activation and culture, it was used for in vitro antibacterial assays, adhesion and invasion experiments, Transwell co-culture experiments, and construction of the animal infection model. Human gastric epithelial GES-1 cells, purchased from the Institute of Microbiology, Chinese Academy of Sciences, were used to establish an in vitro gastric epithelial cell infection model.

2.2 In Vitro Experiments

2.2.1 Determination of the Inhibitory Effect of *B. longum* Bianquejun 19 on *H. pylori* Growth

The agar well diffusion assay was employed to evaluate the inhibitory effects of different components in *B. longum* Bianquejun 19 on *H. pylori* growth, with adjustments made based on the sample types and culture conditions used in this study[12][14]. After two passages of activation, the *H. pylori* suspension was adjusted to 1×10^8 CFU/mL and evenly spread onto the surface of fresh Columbia agar medium. The medium was supplemented with 0.01% 2,3,5-triphenyltetrazolium chloride (TTC) to assist visualization of *H. pylori* growth and inhibition zones. After the bacterial suspension had been fully absorbed, sterile Oxford cups were placed on the surface of the plates, and 100 μL of *B. longum* Bianquejun 19 fermentation supernatant, pH-neutralized fermentation supernatant, bacterial suspension, or lysate supernatant was added separately. The concentration of *B. longum* Bianquejun 19 in all treatment preparations was adjusted to 1×10^8 CFU/mL, and the fermentation and lysate supernatants were prepared from equal volumes of *B. longum* Bianquejun

19 cultures with the same initial bacterial concentration.

After sample addition, the plates were allowed to stand under microaerophilic conditions for 1 h to stabilize the samples, and were then incubated at 37 °C under microaerophilic conditions for 72 h. At the end of incubation, *H. pylori* growth in each treatment group was observed, and the diameter of the inhibition zone was measured. The direct inhibitory effects of different components of *B. longum* Bianquejun 19 on *H. pylori* growth were evaluated by comparing inhibition-zone diameters among treatment groups.

2.2.2 Absorbance-Based Assay for *H. pylori* Adhesion

GES-1 gastric epithelial cells were seeded into 96-well plates at a density of 1×10^4 cells/well and cultured to 80%-90% confluence. The medium was then discarded, and the cells were washed twice with serum-free DMEM. Adhesion-interference experiments were performed using the following three modes: (1) competition mode, in which *H. pylori* suspension and *B. longum* Bianquejun 19 treatment samples were added simultaneously; (2) exclusion mode, in which *B. longum* Bianquejun 19 treatment samples were added and incubated for 2 h, followed by PBS washing and then addition of *H. pylori* suspension; and (3) displacement mode, in which *H. pylori* suspension was first added and incubated for 2 h, followed by PBS washing and addition of *B. longum* Bianquejun 19 treatment samples. The establishment of competition, exclusion, and displacement models refers to the research ideas of previous studies on probiotics interfering with pathogen adhesion, and adjustments are made in combination with the GES-1 cell model used in this study[12][14]. The final concentration of *H. pylori* was 1×10^7 CFU/mL (MOI = 100), and co-culture was conducted for 2-4 h. After incubation, the culture medium was removed, and the cells were gently washed 3-5 times with PBS to thoroughly remove non-adherent bacteria. The cells

were fixed with 4% paraformaldehyde at room temperature for 15 min and air-dried. Subsequently, 100 μL of 0.1% crystal violet solution was added to each well for staining at room temperature for 15-20 min. After excess dye was removed and the plates were air-dried, 33% glacial acetic acid was added and shaken for 10-15 min to dissolve the dye. Absorbance at OD570 nm was measured using a microplate reader. Blank controls containing only cells and positive controls containing only *H. pylori* were included.

Adhesion inhibition rate (%) = [(OD $_{\textit{H. pylori}\ \text{group}}$ - OD $_{\text{treatment group}}$) / OD $_{\textit{H. pylori}\ \text{group}}$] × 100%

2.2.3 Inhibition Assay for *H. pylori* Invasion

The gentamicin protection assay was used to detect bacterial invasion[16]. GES-1 cells were seeded into 24-well plates at a density of 5×10^4 cells/well and cultured to 80% confluence. Invasion-intervention experiments were performed using the following three modes: (1) competition mode, in which *H. pylori* (MOI = 100) and *B. longum* Bianquejun 19 treatment samples were added simultaneously and co-cultured for 4 h; (2) exclusion mode, in which *B. longum* Bianquejun 19 treatment samples were added and incubated for 2 h, followed by PBS washing and subsequent addition of *H. pylori* for another 4 h; and (3) displacement mode, in which *H. pylori* was incubated for 2 h, followed by PBS washing and addition of *B. longum* Bianquejun 19 treatment samples for another 2 h. After each treatment, the cells were washed three times with PBS to remove suspended bacteria and then incubated at 37 °C for 2 h in medium containing 100 μg/mL gentamicin to specifically kill extracellular non-invaded bacteria. The medium was then discarded, and the cells were washed three times with PBS, fixed with 4% paraformaldehyde for 15 min, stained with 0.1% crystal violet for 20 min, washed, dissolved with 33% glacial acetic acid, and measured at OD570 nm to indirectly quantify intracellular bacteria.

Invasion inhibition rate (%) = [(invasive bacterial load in the control group - invasive bacterial load in the treatment group) / invasive bacterial load in the control group] × 100%

2.3 Metatranscriptomic Sequencing and Bioinformatics Analysis

2.3.1 Sample Collection

GES-1 gastric epithelial cells were seeded into 96-well plates at a density of 1×10^4 cells/well and cultured to 80%-90% confluence. The medium was discarded, and the cells were washed twice with serum-free DMEM. *H. pylori* suspension and *B. longum* Bianquejun 19 were then added simultaneously and co-cultured for 4 h. The culture medium was discarded, and pre-cooled PBS (500-1000 μL) was added. Cells and adherent bacteria were scraped off using a cell scraper and thoroughly resuspended. Pre-cooled absolute ethanol was then added at a ratio of 1:3, followed immediately by vigorous vortexing for 10 s and centrifugation at 5000 r/min for 5 min at 4 °C. The supernatant was discarded, and the resulting white, translucent pellet was snap-frozen in liquid nitrogen.

2.3.2 Experimental Procedures

2.3.2.1 RNA Extraction, rRNA Depletion, and Library Construction

Total RNA was extracted using the Soil RNA Extraction Kit (Majorbio, Shanghai, China). After RNA extraction, RNA concentration and purity were determined, RNA integrity was assessed by 1% agarose gel electrophoresis, and RNA quality values were measured using the Agilent 5300 system. rRNA was then removed using the RiboCop rRNA Depletion Kit for Mixed Bacterial Samples (Lexogen, USA) to enrich target mRNA.

After rRNA depletion, transcriptome libraries were constructed using the Illumina® Stranded mRNA Prep, Ligation kit. The main steps included RNA fragmentation, first-strand cDNA

synthesis using random primers, second-strand cDNA synthesis, end repair, A-tailing, adapter ligation, magnetic bead selection, and PCR amplification. The amplified libraries were subjected to quality control and used for subsequent sequencing after meeting the quality requirements.

2.3.2.2 Sequencing and Data Quality Control

Libraries were constructed using Illumina® Stranded mRNA Prep, Ligation (Illumina, USA). After the raw sequencing data were obtained, reads were quality-controlled using fastp software[17]. Adapter sequences at the 3' and 5' ends were removed, and reads with a post-trimming length of <50 bp, an average base quality score of <20, or containing N bases were filtered out, retaining high-quality paired-end reads and single-end reads. SortMeRNA software was subsequently used to align reads against the SILVA SSU (16S/18S) and SILVA LSU (23S/28S) databases to remove reads mapped to rRNA, generating high-quality non-rRNA sequences for subsequent analysis.

All data analyses were performed on the Majorbio Cloud Platform[18].

2.3.2.3 Sequencing and Data Quality Control

The quality-controlled sequences were assembled using MEGAHIT (v.4.6.1)[19], and contigs with lengths ≥500 bp were retained. Open reading frames (ORFs) were then predicted using Prodigal (v.2.6.3)[20]. Gene sequences with nucleotide lengths ≥100 bp were selected and translated into amino acid sequences.

Predicted ORFs were clustered and dereplicated using CD-HIT with parameters of 95% identity and 90% coverage. The longest sequence in each cluster was selected as the representative sequence to construct a non-redundant unigene set for subsequent taxonomic annotation, functional annotation, and expression-abundance analysis.

2.3.2.4 Calculation of Gene Expression and Definition of TPM

Clean reads were aligned against the non-redundant unigene set, and the expression abundance of each gene was quantified using RSEM. Transcripts per million (TPM) was used as the normalized measure of gene transcript abundance. TPM normalizes transcript counts for both gene length and sequencing depth, making it suitable for comparing the transcript abundance of the same gene across different samples. In subsequent analyses, changes in the expression of genes related to central carbon metabolism, oxidative phosphorylation, flagellar assembly, motility, and virulence were expressed as TPM values.

2.3.2.5 Taxonomic, Functional, and Virulence-Factor Annotation

The amino acid sequences of the unigene set were aligned against the NR database using Diamond BLASTP[21], and taxonomic annotation results were obtained based on the corresponding classification information in the NR database. Species expression abundance was calculated as the sum of TPM abundance values for genes assigned to that species.

GO functional annotation was also performed using Diamond[21], and the abundance of each GO functional category was calculated based on the expression abundance of related genes. COG functional annotation was obtained by aligning the amino acid sequences of the unigene set against the eggNOG database. KEGG functional annotation was performed by aligning the unigene set against the KEGG GENES database using Diamond, followed by KO, pathway, EC, and module annotation using KOBAS software.

Virulence-factor annotation was performed by aligning amino acid sequences from the non-redundant gene set against the VFDB core database using Diamond[21]. Sequences that failed to align were further compared with the VFDB predicted database to obtain annotation information

for *H. pylori* virulence-related genes.

2.4 Determination of *H. pylori* Acetyl-CoA, ATP, and NADH/NAD+ Contents

2.4.1 Establishment of the Co-Culture System

A Transwell co-culture system was used to physically separate the probiotic and *H. pylori* while allowing the exchange of soluble metabolites and signaling molecules. Sterile 6-well Transwell inserts with 0.4 μm polycarbonate membranes were placed in matched culture plates.

H. pylori was inoculated into the lower chamber in brain heart infusion (BHI) medium containing 10% fetal bovine serum and cultured at 37 °C under microaerophilic conditions (5% O_2, 10% CO_2, and 85% N_2). Before inoculation, the bacterial density was adjusted to approximately 1×10^8 CFU/mL.

2.4.2 Preparation of the Probiotic Suspension

Probiotic cells were collected by centrifugation, washed with sterile phosphate-buffered saline (PBS), and resuspended in fresh MRS medium at a density of approximately 1×10^8 CFU/mL. The probiotic suspension was added to the upper chamber, yielding a *H. pylori*-to-probiotic ratio of approximately 1:20-1:50. To maintain probiotic activity under microaerophilic conditions, L-cysteine was added to the medium at a final concentration of 0.05% (w/v) to reduce oxidative stress and stabilize the redox environment of the co-culture system. Samples for metabolite measurements were collected at 0, 1, 2, 3, 4, 8, 12, and 24 h, whereas samples for motility assays and morphological observations were collected at 0, 4, 8, 12, and 24 h according to the experimental design.

2.4.3 Collection of *H. pylori* Samples

At the end of each time point, the Transwell insert containing the probiotic was carefully removed using sterile forceps to avoid disturbing the lower chamber. The culture medium in the lower chamber was immediately aspirated and centrifuged at 4000 × g for 5 min at 4 °C to rapidly collect *H. pylori* cells, which were washed once with pre-cooled PBS.

2.4.4 Extraction and Determination of Intracellular Metabolites

To preserve intracellular metabolites, the washed bacterial pellet was immediately resuspended in pre-cooled 60% methanol (-20 °C), incubated on ice for 5 min, and then centrifuged at 12000 × g for 5 min at 4 °C. The resulting pellet was used to determine intracellular adenosine triphosphate (ATP), reduced nicotinamide adenine dinucleotide (NADH) and its oxidized form (NAD^+), and acetyl-coenzyme A (acetyl-CoA) according to the instructions of the corresponding commercial kits. The kits used included the Coenzyme I NAD(H) Assay Kit (Cat. No. A114-1-1, Nanjing Jiancheng Bioengineering Institute), the ATP Assay Kit (Cat. No. A095-1-1, 100T/48 samples, Batch No. 2C260420, Nanjing Jiancheng Bioengineering Institute), and the Acetyl-CoA Assay Kit (Cat. No. BC0980, 25T/24 samples, Batch No. 2603002002, Solarbio).

2.4.5 Evaluation of Motility by Soft-Agar Stab Assay

Fresh Columbia agar medium containing antibiotics was prepared, sterilized, and supplemented with 10% fetal bovine serum and 0.01% (w/v) TTC. The medium was mixed thoroughly and poured into plates. After solidification, the plates were inverted and incubated overnight at 37 °C. The *H. pylori* cells collected after co-culture as described in Section 2.4.3 were resuspended, and the bacterial suspension was inoculated into the center of the soft agar using an inoculating needle by vertical stabbing to a depth of approximately two-thirds of the agar

thickness. Four to six evenly distributed stab sites were inoculated per plate. The plates were incubated at 37 °C under microaerophilic conditions for 7 days, after which the radius of the motility halo was measured in millimeters.

2.5 Transmission Electron Microscopy (TEM)

H. pylori samples after co-culture were collected according to the methods described in Sections 2.4.1, 2.4.2, and 2.4.3. At each culture time point, the Transwell insert in the upper chamber was gently removed with sterile forceps to avoid shaking or disturbing the bacterial suspension in the lower chamber. All culture medium from the lower chamber of the 6-well plate was carefully aspirated into a sterile centrifuge tube. Carbon-coated Formvar copper grids were subjected to glow discharge treatment and then placed film-side down onto droplets of the collected *H. pylori* suspension for adsorption for 3-5 min. After adsorption, excess bacterial suspension was gently removed from the edge of the grid using filter paper, and the grid was transferred to 1% phosphotungstic acid stain for negative staining for 40-60 s. After staining, the grids were rinsed sequentially with sterile ultrapure water and air-dried at room temperature in the dark.

The dried samples were observed under a transmission electron microscope (TEM; HITACHI HT7800). Areas with uniform bacterial distribution, clean background, and no obvious staining precipitates were first selected under low magnification, followed by gradual increases in magnification to observe and capture images of *H. pylori* cell morphology, cellular outline, surface integrity, and flagellar structure. For each group, 5-10 representative fields were randomly selected for imaging to compare *H. pylori* cell integrity and flagellar morphology after *B. longum* Bianquejun 19 treatment.

2.6 In Vivo Experiments

The mouse infection modeling protocol follows the classical H. pylori mouse infection model and is adjusted according to the experimental strain, animal lineage, and intervention duration of this study[22]. Eight-week-old male specific pathogen-free (SPF) C57BL/6 mice (n = 10 per group) were used in this study. All mice were acclimatized for 7 days before model establishment. The infection modeling period lasted from Day 8 to Day 21. Prior to intragastric administration, the mice were fasted for 12 hours. Each mouse was first given 0.2 mL of sodium bicarbonate solution via gavage. After a 30-minute interval, 0.2 mL of *H. pylori* bacterial suspension at a concentration of 1×10^8 CFU/mL was administered intragastrically. Gavage was performed once every two days for a total of 2 weeks. Mice in the control group were fasted for 12 hours before receiving 0.2 mL of 0.9% normal saline by gavage.

Following infection, all mice were maintained under routine feeding conditions for 1 week (Day 22 to Day 28) to allow bacterial colonization, after which subsequent interventions were initiated. The intervention period of Bianque Jun 19 lasted from Day 29 to Day 70. The model mice were randomly divided into four groups: model group (administered 0.2 mL of 0.9% normal saline), combined antibiotic group (containing 0.025 μg/mL omeprazole, 0.125 μg/mL amoxicillin, and 0.5 μg/mL metronidazole, 0.2 mL per mouse), and probiotic groups treated with Bianque Jun 19. The probiotic groups were further subdivided into bacterial suspension group, supernatant group, and lysed supernatant group, all of which were given 0.2 mL of treatment solution at a concentration of 5×10^8 CFU/mL.

All animal experiments complied with relevant national laws, regulations, and institutional guidelines. This study was approved by the Animal Ethics Committee of Beijing University of

Agriculture (Approval No.: GSCS-2025-018; Approval Date: July 28, 2025).

2.6.1 Sample Collection and Processing

At the experimental endpoint, mice were fasted for 12 h and then anesthetized and euthanized. After euthanasia, colonic fecal contents were collected, immediately snap-frozen in liquid nitrogen, and then stored at -80 °C for short-chain fatty acid analysis.

Whole blood was collected to separate serum for ELISA detection of inflammatory factors. Blood was collected by eyeball removal and allowed to stand at room temperature for 2 h, followed by centrifugation at 3000 rpm for 15 min. The upper serum layer was collected, aliquoted, and stored at -80 °C until use.

Gastric tissues were aseptically collected, opened along the greater curvature, and rinsed with cold PBS to remove gastric contents. The tissues were then divided into portions: one portion was snap-frozen in liquid nitrogen, and another portion was fixed in 4% paraformaldehyde.

2.6.2 Histopathological Examination (H&E and Masson Staining)

Fixed gastric tissues were dehydrated through graded ethanol, cleared in xylene, embedded in paraffin, and sectioned into continuous 4-5 μm slices.

H&E staining: Sections were routinely stained with hematoxylin and eosin (H&E), and gastric mucosal inflammatory-cell infiltration, epithelial exfoliation, and structural integrity were observed under a light microscope.

Masson staining: Sections were stained using Masson trichrome staining, and collagen fiber deposition was observed microscopically (collagen fibers appeared blue and muscle fibers appeared red). The collagen-positive area was semi-quantitatively analyzed using ImageJ software to evaluate the effects of *H. pylori* infection and the different interventions on gastric collagen

deposition and tissue remodeling[23].

2.6.3 Detection of Short-Chain Fatty Acids (SCFAs) in Colonic Contents

The concentrations of acetate, valerate, isobutyrate, and isovalerate in colonic contents were determined by gas chromatography–mass spectrometry (GC–MS)[24]. Frozen samples were subjected to acidified extraction and organic-solvent extraction before instrumental analysis. The absolute concentration of each SCFA was calculated using the corresponding standard curve.

2.6.4 Detection of Serum Inflammatory Factors and the cagA Virulence Factor

The serum levels of TNF-α, IL-1β, IL-6, TGF-β, IL-10, and IFN-γ in each group, as well as CagA protein levels in gastric tissue homogenates, were measured using enzyme-linked immunosorbent assay (ELISA) kits. All procedures were performed strictly according to the manufacturer's instructions. Diluted serum or gastric tissue homogenate samples were added to the pre-coated microplate wells, followed sequentially by enzyme-conjugated antibodies and chromogenic substrate solution. Absorbance was measured at 450 nm using a microplate reader, and the concentration of each analyte was calculated from the corresponding standard curve.

2.7 Statistical Analysis

Data are presented as the mean ± standard error of the mean (mean ± SEM). Comparisons between two groups were performed using an independent-samples t-test. Comparisons among three or more groups were conducted using one-way analysis of variance, followed by an appropriate multiple-comparison test. A value of $p < 0.05$ was considered statistically significant. Different lowercase letters in the figures indicate significant differences among groups.

3 Results

3.1 In vitro antibacterial activity and intervention effects on adhesion and invasion

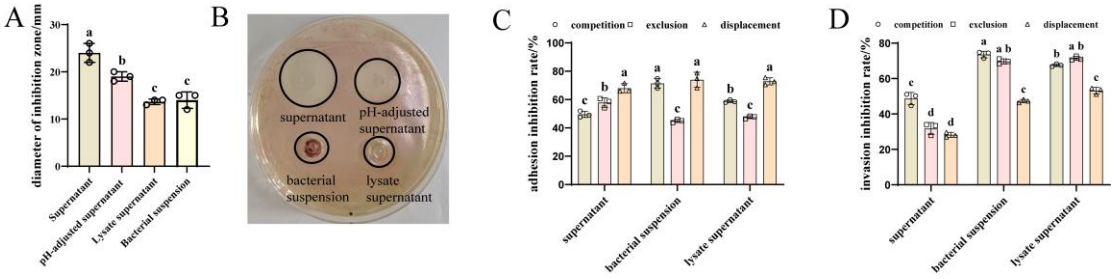


Fig. 1 Effects of different components of *B. longum* Bianquejun 19 on the antibacterial activity, adhesion, and invasion capacity of *H. pylori*. A-B: inhibition-zone assay results showing the inhibition-zone diameters of *H. pylori* under different component treatments; C: inhibitory effects of each component on *H. pylori* adhesion to GES-1 gastric epithelial cells under different treatment modes; D: inhibitory effects of each component on *H. pylori* invasion of GES-1 cells under different treatment modes.

Note: Different lowercase letters indicate significant differences between groups ($p < 0.05$).

Fig. 1 shows the effects of different components of *B. longum* Bianquejun 19 on *H. pylori* growth, adhesion, and invasion. The inhibition-zone assay showed that the fermentation supernatant group produced the largest inhibition zone, with an average diameter of 24.00 mm. The inhibition-zone diameter of the pH-neutralized fermentation supernatant group was 19.00 mm, which was significantly smaller than that of the non-neutralized fermentation supernatant group ($p < 0.05$). The inhibition-zone diameters of the live-cell suspension group and lysate supernatant group were 14.00 mm and 13.67 mm, respectively, both of which were significantly smaller than that of the pH-neutralized fermentation supernatant group ($p < 0.05$).The live bacterial suspension formed a clear TTC reduction zone around the wells, and the measurement of the apparent inhibition zone diameter was combined with the competition of bacterial red zone

388 boundaries, with an average of 14.00 mm.

389 The adhesion assay results are shown in Fig. 1C. Different lowercase letters in the figure
390 indicate significant differences among the competition, exclusion, and displacement modes within
391 the same component ($p < 0.05$). For the fermentation supernatant group, the adhesion inhibition
392 rate in the displacement mode (67.98%±1.84%) was significantly higher than that in the
393 competition (49.51%±1.23%) and exclusion (57.88%±1.96%) modes ($p < 0.05$). For the
394 bacterial suspension group, the inhibition rate in the competition mode reached 71.41%±1.98%,
395 and the inhibition rates in both the competition and displacement modes (73.95%±3.08%) were
396 significantly higher than that in the exclusion mode (44.94%±0.67%) ($p < 0.05$). For the lysate
397 group, the inhibition rate in the displacement mode (72.89%±1.44%) was significantly higher
398 than those in the competition and exclusion modes ($p < 0.05$).

399 The invasion assay results are shown in Fig. 1D. For the fermentation supernatant group, the
400 invasion inhibition rate in the competition mode was significantly higher than that in the exclusion
401 and displacement modes ($p < 0.05$), peaking at 48.71%±2.01%. For the bacterial suspension
402 group, the inhibition rate in the competition mode reached 73.57%±1.09%, and the inhibition rate
403 in the exclusion mode also remained high (69.67%±0.85%); both were significantly higher than
404 that in the displacement mode (47.31%±0.55%) ($p < 0.05$). For the lysate group, the inhibition
405 rate in the exclusion mode was the highest (71.37%±0.67%) and was significantly higher than
406 those in the competition (67.60%±0.44%) and displacement (53.16%±1.07%) modes ($p < 0.05$).

3.2Transcriptomic and Physiological Responses of *H. pylori* after *B. longum* Bianquejun 19 Treatment

3.2.1Expression Changes in Genes Related to Carbon Metabolism and Acetyl-CoA Homeostasis

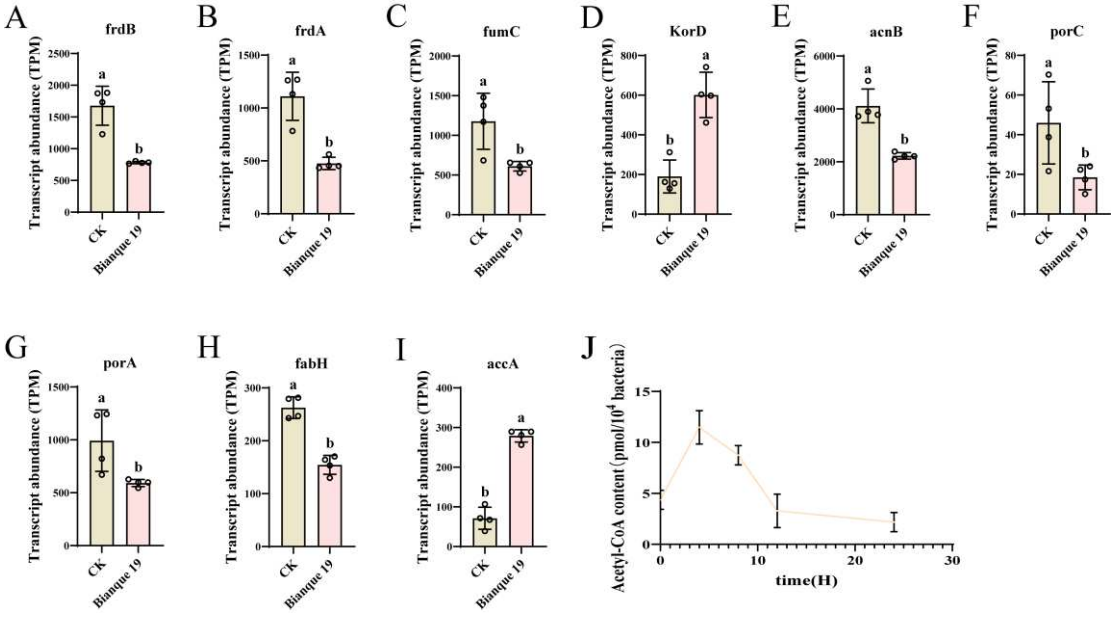


Fig. 2 Effects of *B. longum* Bianquejun 19 treatment on the transcriptional levels of central carbon metabolism-related genes and intracellular acetyl-CoA content in *H. pylori*. A-I: transcriptional abundance (TPM) of frdB, frdA, fumC, KorD, acnB, porC, porA, fabH, and accA; J: dynamic changes in intracellular acetyl-CoA content.

Note: Different lowercase letters indicate significant differences between groups ($p < 0.05$).

Fig. 2 shows the effects of *B. longum* Bianquejun 19 treatment on the transcriptional levels of genes related to central carbon metabolism and intracellular acetyl-CoA content in *H. pylori*. frdB (Fig. 2A) and frdA (Fig. 2B) encode subunits related to the fumarate reductase complex and participate in fumarate reduction and anaerobic electron transport. Compared with the control group, *B. longum* Bianquejun 19 treatment significantly downregulated frdB expression by approximately 2.15-fold and frdA expression by approximately 2.33-fold ($p < 0.05$).

fumC (Fig. 2C) encodes fumarate hydratase, which participates in the interconversion

423 between fumarate and malate. The results showed that fumC expression was significantly
424 downregulated by approximately 1.93-fold after *B. longum* Bianquejun 19 treatment ($p < 0.05$).
425 KorD (Fig. 2D) is a gene related to the 2-oxoglutarate oxidoreductase complex and participates in
426 2-oxoglutarate metabolism. Compared with the control group, KorD expression was significantly
427 upregulated by approximately 3.16-fold ($p < 0.05$).
428 acnB (Fig. 2E) encodes aconitate hydratase, which participates in the conversion of citrate to
429 isocitrate and is an important enzyme in the early phase of the TCA cycle. The results showed that
430 acnB expression was significantly downregulated by approximately 1.85-fold after *B. longum*
431 Bianquejun 19 treatment ($p < 0.05$). porC (Fig. 2F) and porA (Fig. 2G) encode subunits related to
432 the pyruvate: ferredoxin oxidoreductase complex, which participates in the oxidative
433 decarboxylation of pyruvate to acetyl-CoA. After treatment, porC expression was significantly
434 downregulated by approximately 2.49-fold and porA expression by approximately 1.68-fold ($p <$
435 0.05).
436 fabH (Fig. 2H) participates in the initiation reaction of fatty acid synthesis and is related to
437 acetyl-CoA and lipid biosynthetic metabolism. The results showed that fabH expression was
438 significantly downregulated by approximately 1.70-fold after *B. longum* Bianquejun 19 treatment
439 ($p < 0.05$). accA (Fig. 2I) encodes a subunit related to acetyl-CoA carboxylase and participates in
440 the conversion of acetyl-CoA to fatty acid synthesis precursors. Compared with the control group,
441 accA expression was significantly upregulated by approximately 3.91-fold ($p < 0.05$).
442 The results of acetyl-CoA content measurement are shown in Fig. 2J. Acetyl-CoA is a key
443 hub molecule linking pyruvate metabolism, the TCA cycle, fatty acid synthesis, and energy
444 metabolism. The results showed that after *B. longum* Bianquejun 19 treatment, intracellular acetyl-

CoA content in *H. pylori* displayed a dynamic pattern of initial increase followed by a decrease. At 0 h, acetyl-CoA content was approximately 4.37 pmol/10^4 bacteria. After 4 h of treatment, it increased to approximately 11.48 pmol/10^4 bacteria, approximately 2.62 times the 0 h level. At 8 h, acetyl-CoA content remained relatively high at 8.75 pmol/10^4 bacteria, approximately 2.00 times the 0 h level. As treatment time increased, acetyl-CoA content gradually decreased, falling to 3.28 pmol/10^4 bacteria at 12 h and further to 2.19 pmol/10^4 bacteria at 24 h, below the initial level.

3.2.2 Disruption of Respiratory Chain Function, ATP Synthesis, and Redox Homeostasis

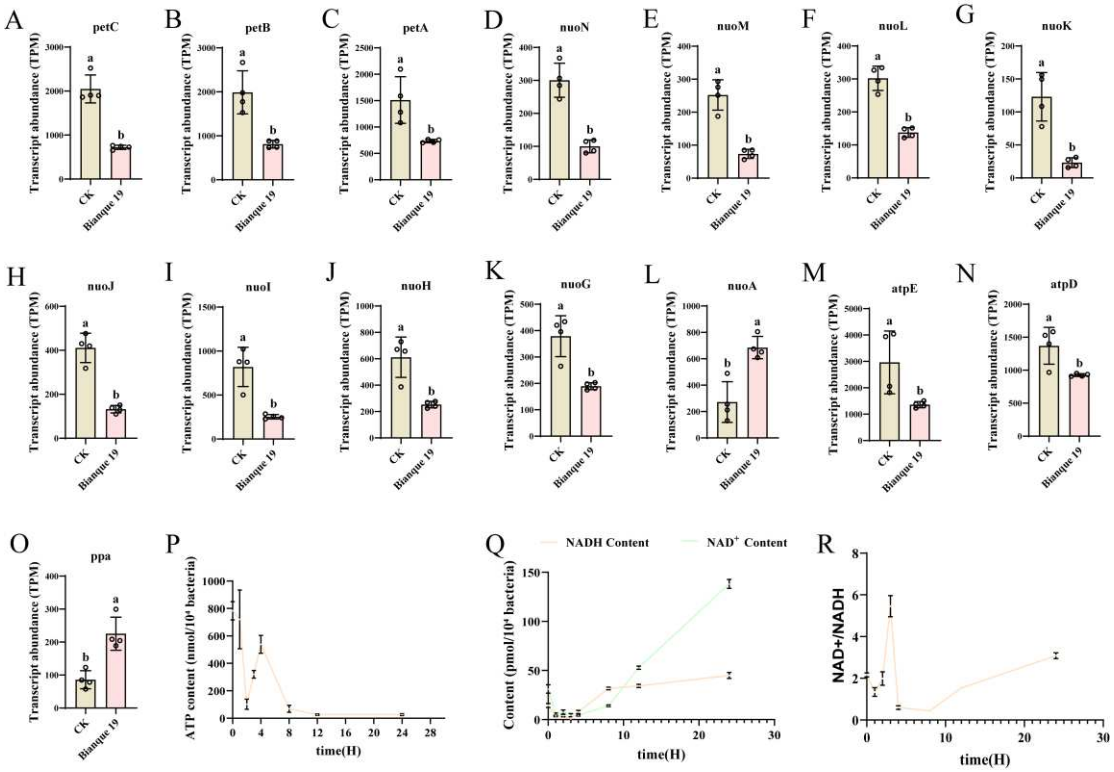


Fig. 3 Dynamic changes in oxidative phosphorylation pathway gene expression, intracellular energy metabolites, and redox homeostasis in *H. pylori* after *B. longum* Bianquejun 19 treatment. A-C: transcriptional levels of petA, petB, and petC encoding cytochrome bc_1 complex subunits; D-L: transcriptional levels of nuo family genes related to respiratory-chain complex I; M-N: transcriptional levels of atpE and atpD encoding ATP synthase subunits; O:

transcriptional level of ppa encoding inorganic pyrophosphatase; P: changes in intracellular ATP content in *H. pylori* at different treatment times; Q-R: changes in intracellular NAD^+ and NADH contents and the NAD^+/NADH ratio at different treatment times.

Note: Different lowercase letters indicate significant differences between groups ($p < 0.05$).

Fig. 3 shows the effects of *B. longum* Bianquejun 19 treatment on oxidative phosphorylation-related gene expression, ATP content, and NADH/NAD^+ homeostasis in *H. pylori*. petC (Fig. 3A), petB (Fig. 3B), and petA (Fig. 3C) encode cytochrome bc_1 complex-related subunits and participate in electron transport in the respiratory chain. Compared with the control group, *B. longum* Bianquejun 19 treatment significantly downregulated petA expression by approximately 2.06-fold, petB expression by approximately 2.45-fold, and petC expression by approximately 2.84-fold ($p < 0.05$).

nuoN (Fig. 3D), nuoM (Fig. 3E), nuoL (Fig. 3F), nuoK (Fig. 3G), nuoJ (Fig. 3H), nuoI (Fig. 3I), and nuoH (Fig. 3J) are genes related to NADH dehydrogenase complex I and participate in NADH oxidation, electron transport, and proton translocation. The results showed that nuoN expression was significantly downregulated by approximately 3.01-fold; nuoM by approximately 3.42-fold; nuoL by approximately 2.19-fold; nuoK by approximately 5.30-fold; nuoJ by approximately 3.11-fold; nuoI by approximately 3.24-fold; and nuoH by approximately 2.42-fold ($p < 0.05$).

nuoG (Fig. 3K) also belongs to the NADH dehydrogenase complex I-related genes and is mainly associated with electron transfer in the peripheral arm. Compared with the control group, nuoG expression was significantly downregulated by approximately 2.00-fold ($p < 0.05$). nuoA (Fig. 3L) encodes a membrane-associated subunit of complex I, and its expression was

significantly upregulated by approximately 2.52-fold after treatment ($p < 0.05$).

atpE (Fig. 3M) and atpD (Fig. 3N) are ATP synthase-related genes. atpE encodes a proton-channel subunit of the F_0 portion, whereas atpD encodes a catalytic subunit of the F_1 portion responsible for ATP synthesis. After *B. longum* Bianquejun 19 treatment, atpE expression was significantly downregulated by approximately 2.18-fold and atpD expression by approximately 1.48-fold ($p < 0.05$). ppa (Fig. 3O) encodes inorganic pyrophosphatase and participates in inorganic pyrophosphate hydrolysis and phosphate metabolism. The results showed that ppa expression was significantly upregulated by approximately 2.62-fold ($p < 0.05$).

The ATP content results are shown in Fig. 3P. ATP is a critical energy molecule required for bacterial growth, substance transport, flagellar motility, and environmental adaptation. The results showed that at 0 h, intracellular ATP content in *H. pylori* was approximately 783.33 nmol/10^4 bacteria. After 1 h of treatment, ATP content was 720.37 nmol/10^4 bacteria, representing a slight decrease compared with 0 h. After 2 h, ATP content decreased markedly to 101.85 nmol/10^4 bacteria, approximately 13.00% of the 0 h level. At 3 h and 4 h, ATP content recovered to 320.37 and 538.89 nmol/10^4 bacteria, respectively, suggesting some early fluctuations in ATP content. As treatment time was further extended, ATP content decreased again markedly, reaching 68.73 nmol/10^4 bacteria at 8 h, 26.44 ± 3.19 nmol/10^4 bacteria at 12 h, and 26.22 nmol/10^4 bacteria at 24 h, remaining overall at a low level.

Changes in NADH and NAD^+ contents are shown in Fig. 3Q. NADH is an electron donor for the respiratory chain, whereas NAD^+ is its oxidized form; together, they reflect cellular redox status. NADH content was 14.44 pmol/10^4 bacteria at 0 h and decreased to 3.66, 3.90, and 0.82 pmol/10^4 bacteria after 1, 2, and 3 h of treatment, respectively; it then increased to 7.65 pmol/10^4

503 bacteria at 4 h. Subsequently, NADH content increased markedly, reaching 31.67, 34.32, and
504 44.96 pmol/10^4 bacteria at 8, 12, and 24 h, respectively. NAD^+ content was 31.19 pmol/10^4
505 bacteria at 0 h and decreased to 5.01, 7.70, 4.48, and 4.48 pmol/10^4 bacteria after 1, 2, 3, and 4 h
506 of treatment, respectively; it was 14.10 pmol/10^4 bacteria at 8 h. After 12 and 24 h of treatment,
507 NAD^+ content increased markedly to 52.80 and 138.24 pmol/10^4 bacteria, respectively.
508 Changes in the NAD^+/NADH ratio are shown in Fig. 3R. At 0 h, the NAD^+/NADH ratio was
509 2.16; after 1 and 2 h of treatment, it was 1.34 and 1.99, respectively. At 3 h, the NAD^+/NADH
510 ratio increased to 5.46, the highest value among all time points. It then decreased markedly at 4
511 and 8 h, to 0.59 and 0.45, respectively. At 12 h, the NAD^+/NADH ratio recovered to 1.54 and
512 further increased to 3.08 at 24 h. These results indicate that ATP content, NADH/NAD^+ levels, and
513 the NAD^+/NADH ratio in *H. pylori* underwent marked time-dependent changes after *B. longum*
514 Bianquejun 19 treatment.

3.2.3 Changes in the expression of genes related to flagellar assembly, motility, and virulence

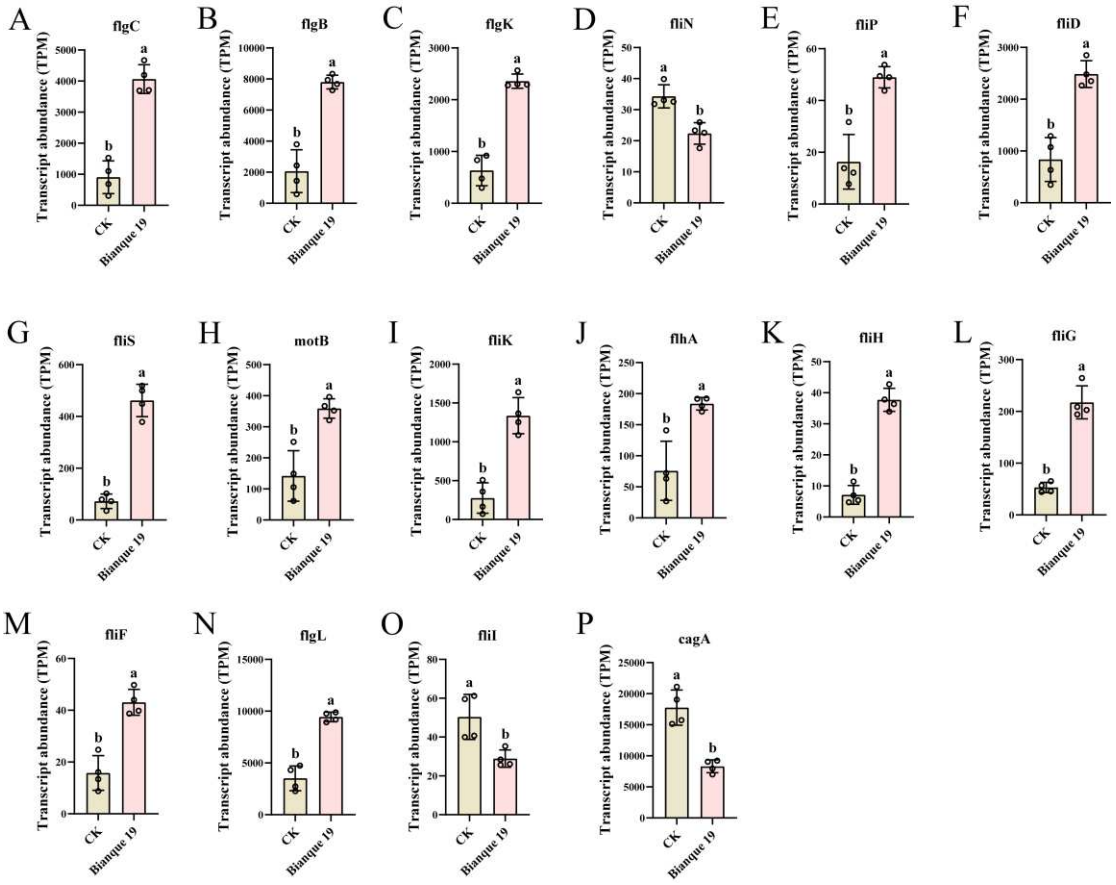


Fig. 4 Effects of *B. longum* Bianquejun 19 treatment on the transcriptional abundance of flagellar-system-related genes and the virulence-associated gene cagA in *H. pylori*. A-O correspond sequentially to the transcriptional levels of flgC, flgB, flgK, fliN, fliP, fliD, fliS, motB, fliK, flhA, fliH, fliG, fliF, flgL, and fliI. P: Transcriptional abundance of the virulence-associated gene cagA.

Note: Different lowercase letters indicate significant differences between groups ($p < 0.05$).

Fig. 4 shows the effects of *B. longum* Bianquejun 19 treatment on the transcriptional levels of *H. pylori* flagellar-system-related genes. flgC (Fig. 4A) and flgB (Fig. 4B) are both involved in formation of the flagellar basal-body rod structure. Compared with the control group, flgC expression was significantly upregulated by approximately 4.49-fold and flgB expression by

527 approximately 3.78-fold ($p < 0.05$).

528 flgK (Fig. 4C) and flgL (Fig. 4N) participate in formation of the flagellar hook-filament
529 junction. The results showed that flgK expression was significantly upregulated by approximately
530 3.73-fold and flgL expression by approximately 2.69-fold ($p < 0.05$). fliD (Fig. 4F) participates in
531 assembly of the flagellar filament cap, and its expression was significantly upregulated by
532 approximately 2.97-fold after treatment ($p < 0.05$). fliS (Fig. 4G) is a flagellar protein chaperone-
533 related gene involved in flagellar protein stability and export; its expression was significantly
534 upregulated by approximately 6.39-fold ($p < 0.05$).

535 fliP (Fig. 4E), flhA (Fig. 4J), fliH (Fig. 4K), and fliK (Fig. 4I) are all associated with the
536 flagellar export apparatus or flagellar assembly. Specifically, fliP participates in transmembrane
537 transport of flagellar proteins, flhA is an important component of the flagellar export apparatus,
538 fliH is related to the function of the flagellar export ATPase complex, and fliK participates in
539 regulation of flagellar hook length. After *B. longum* Bianquejun 19 treatment, fliP expression was
540 significantly upregulated by approximately 3.00-fold; flhA by approximately 2.42-fold; fliH by
541 approximately 5.29-fold; and fliK by approximately 4.84-fold ($p < 0.05$).

542 motB (Fig. 4H), fliF (Fig. 4M), and fliG (Fig. 4L) are related to the flagellar motor and basal-
543 body structure. Among them, motB is a flagellar motor stator-related gene, fliF participates in MS-
544 ring formation, and fliG is associated with the motor rotor and regulation of motility direction.
545 The results showed that motB expression was significantly upregulated by approximately 2.53-
546 fold; fliF by approximately 2.73-fold; and fliG by approximately 4.10-fold ($p < 0.05$).

547 In contrast to the upregulation of most genes related to flagellar structure and assembly, fliN
548 (Fig. 4D) and fliI (Fig. 4O) were significantly downregulated after *B. longum* Bianquejun 19

treatment. fliN is an important component of the flagellar switch complex and participates in regulation of flagellar rotation direction and chemotactic motility; its expression was significantly downregulated by approximately 1.53-fold ($p < 0.05$). fliI encodes the flagellar export system ATPase, a key energy enzyme involved in flagellar protein export across the membrane and assembly; its expression was significantly downregulated by approximately 1.74-fold ($p < 0.05$).

cagA (Fig. 4P) encodes CagA, an important virulence protein of *H. pylori*. The expression level in the Bianquejun No.19 treatment group decreased by 53.22% compared with the control group, equivalent to a downregulation of approximately 2.14-fold, and the difference was statistically significant ($p<0.05$).

3.2.4 Changes in *H. pylori* Motility and Flagellar Morphology

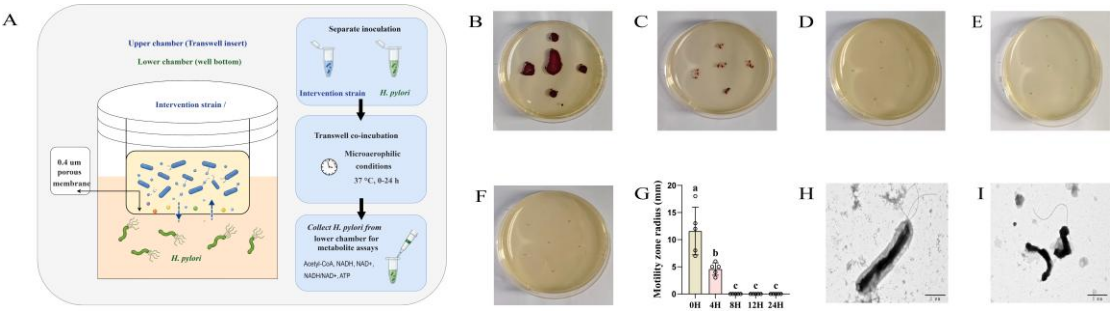


Fig. 5 Effects of *B. longum* Bianquejun 19 treatment on *H. pylori* motility and flagellar morphology. A: schematic diagram of the Transwell co-culture system used to establish a non-contact intervention model; B-F: soft-agar stab assay showing swimming halos of *H. pylori* at different culture times (0, 4, 8, 12, and 24 h); G: quantitative statistics of swimming halo radius; H-I: flagellar morphology of *H. pylori* observed by transmission electron microscopy (H: control group; I: *B. longum* Bianquejun 19 treatment group).

Note: Different lowercase letters indicate significant differences between groups ($p < 0.05$).

Fig. 5 shows the effects of *B. longum* Bianquejun 19 treatment on *H. pylori* motility and flagellar morphology. Fig. 5A presents the schematic diagram of the Transwell co-culture system,

568 which was used to establish a co-culture model in which the probiotic and *H. pylori* were
569 physically separated but soluble metabolites could be exchanged. As shown in Fig. 5B, the control
570 group (0 h) exhibited an obvious swimming halo with an average radius of 11.6 mm (Fig. 5G).
571 After 4 h of *B. longum* Bianquejun 19 intervention (Fig. 5C), the swimming halo radius decreased
572 significantly to 4.6 mm (Fig. 5G) ($p < 0.05$). With prolonged treatment, no obvious swimming
573 halo was observed in the 8 h, 12 h, and 24 h treatment groups (Fig. 5D-F), indicating that the
574 motility and diffusion capacity of *H. pylori* decreased markedly with treatment time.
575 The transmission electron microscopy results are shown in Fig. 5H-I. Fig. 5H shows the
576 morphology of *H. pylori* in the control group. Bacteria in the control group displayed typical rod-
577 shaped or curved rod-shaped morphology, clear cellular outlines, relatively intact cellular
578 structures, and multiple complete, slender flagella at the bacterial poles. Fig. 5I shows the
579 morphology of *H. pylori* in the *B. longum* Bianquejun 19 treatment group. After treatment,
580 bacterial morphology was markedly altered, with visible twisting and breakage of bacterial cells,
581 blurred cell edges, and uneven intracellular electron-density distribution. In addition, the number
582 of flagella was reduced, and incomplete flagella or flagellar structures detached from the bacterial
583 cell were observed.

3.3 In Vivo Experimental Results

3.3.1 Analysis of Pathological Changes in Gastric Tissues

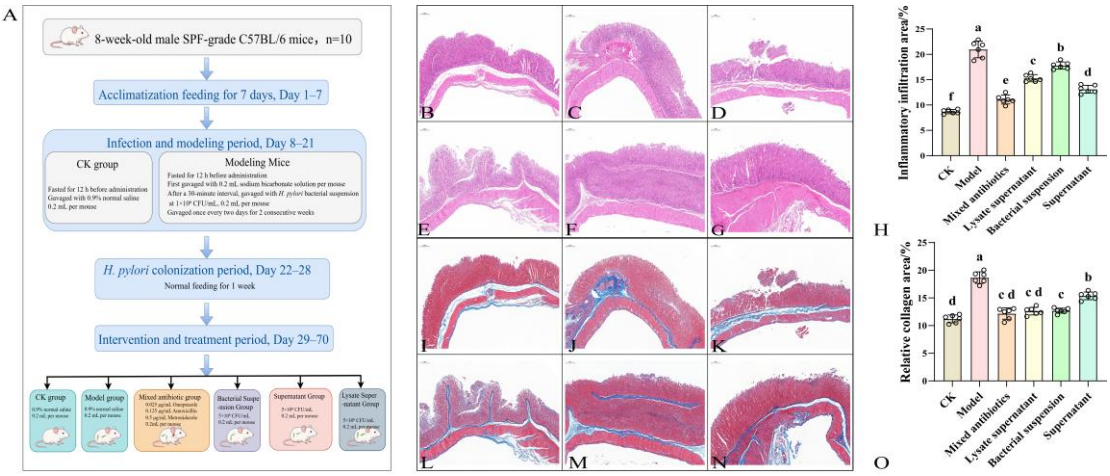


Fig. 6 Effects of different components in *B. longum* Bianquejun 19 on gastric mucosal inflammatory infiltration and collagen deposition in *H. pylori*-infected mice. A: Schematic diagram of animal experimental design; B–G: H&E staining of gastric tissues; H: Statistical analysis of the relative area of inflammatory infiltration. I–N: Masson staining of gastric tissues; O: Statistical analysis of the relative area of collagen fibers. B, I: Blank control group; C, J: *H. pylori* infection model group; D, K: Combined antibiotic group; E, L: Fermented supernatant group; F, M: Bacterial suspension group; G, N: Lysed supernatant group.

Note: Different lowercase letters indicate significant differences between groups ($p < 0.05$).

Fig. 6A shows the schematic workflow of *H. pylori* infection modeling in mice, illustrating the effects of different treatments on inflammatory infiltration and collagen deposition in the gastric mucosa of *H. pylori*-infected model mice. Fig. 6B-G presents H&E staining results, which were used to observe gastric mucosal structural integrity, epithelial injury, and inflammatory-cell infiltration; Fig. 6H shows the quantitative results of inflammatory infiltration area percentage. H&E staining showed that the blank control group (Fig. 6B) had an intact gastric mucosal structure, continuous epithelial cells, regularly arranged glands, and only a small number of

scattered inflammatory cells in the lamina propria and submucosa. Quantitative analysis showed that the inflammatory infiltration area in the control group was 8.70% ± 0.38%. In the *H. pylori* infection model group (Fig. 6C), the gastric mucosa exhibited obvious injury, including mucosal epithelial shedding, erosion, disordered glandular arrangement, and increased inflammatory-cell infiltration in the lamina propria and submucosa. The inflammatory infiltration area increased significantly to 20.96% ± 1.68%, which was significantly higher than that in the control group ($p < 0.05$). After different interventions, the inflammatory infiltration areas of all intervention groups were significantly lower than that of the model group ($p < 0.05$). The inflammatory infiltration area was 11.08% ± 0.97% in the mixed antibiotics group (Fig. 6D), 13.11% ± 0.79% in the fermentation supernatant group (Fig. 6E), 17.79% ± 0.76% in the bacterial suspension group (Fig. 6F), and 15.28% ± 0.70% in the lysate supernatant group (Fig. 6F). Among these, the mixed antibiotics group and fermentation supernatant group showed more pronounced reductions in inflammatory infiltration area.

Fig. 6I-N shows Masson staining results for gastric tissues, which were used to observe collagen fiber deposition; blue areas represent collagen fibers. Fig. 6O presents the quantitative results for relative collagen fiber area. In the control group (Fig. 6I), only a small amount of collagen fibers was observed in the submucosa and around blood vessels, with a collagen area of 11.04% ± 0.79%. In the model group (Fig. 6J), collagen fibers increased markedly, and the collagen area rose significantly to 18.67% ± 1.07%, which was significantly higher than that in the control group ($p < 0.05$). Collagen areas in all intervention groups were significantly lower than that in the model group ($p < 0.05$). The collagen area was 12.17% ± 1.04% in the mixed antibiotics group (Fig. 6K), 15.36% ± 0.68% in the fermentation supernatant group (Fig. 6L),

12.69% ± 0.54% in the bacterial suspension group (Fig. 6M), and 12.61% ± 0.71% in the lysate supernatant group (Fig. 6N). Among these, the mixed antibiotics group, bacterial suspension group, and lysate supernatant group showed more pronounced reductions in collagen area.

3.3.2 Analysis of Short-Chain Fatty Acid (SCFA) Contents in Colonic Contents

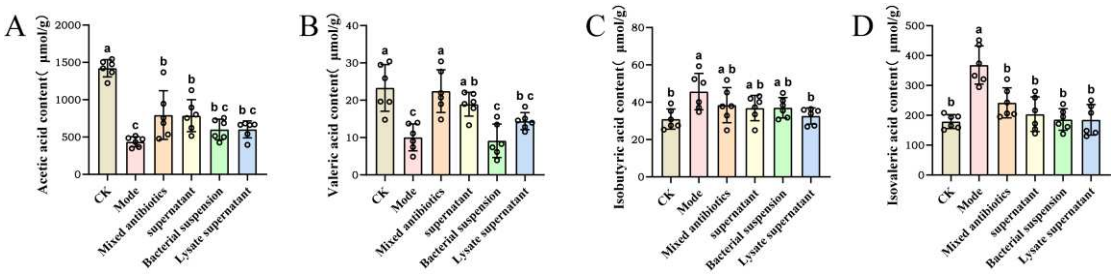


Fig. 7 Effects of different treatments on short-chain fatty acid contents in the colonic contents of *H. pylori*-infected mice. A: acetic acid; B: valeric acid; C: isobutyric acid; D: isovaleric acid.

Note: Different lowercase letters indicate significant differences between groups ($p < 0.05$).

Fig. 7 shows the effects of different treatments on short-chain fatty acid contents in the colonic contents of *H. pylori*-infected mice.

Fig. 7A shows changes in acetic acid content. Acetic acid is one of the major short-chain fatty acids present at high levels in the intestine and is associated with intestinal metabolic status and mucosal barrier function. The results showed that acetic acid content in the blank control group was 1422.24 ± 115.78 μmol/g, whereas it decreased significantly to 436.63 ± 67.77 μmol/g in the *H. pylori* infection model group, which was significantly lower than that in the control group ($p < 0.05$). After intervention, acetic acid content was 794.83 ± 326.29 μmol/g in the mixed antibiotics group, 786.44 ± 214.38 μmol/g in the fermentation supernatant group, 601.28 ± 137.49 μmol/g in the bacterial suspension group, and 602.14 ± 113.06 μmol/g in the lysate supernatant group. Among these, the mixed antibiotics group and fermentation supernatant group had significantly higher acetic acid levels than the model group ($p < 0.05$), whereas the bacterial suspension and

643 lysate supernatant groups showed increases compared with the model group, but the differences
644 were not significant.
645 Fig. 7B shows changes in valeric acid content. Valeric acid is a short-chain fatty acid that can
646 reflect changes in gut microbial metabolites. The results showed that valeric acid content in the
647 blank control group was 23.30 ± 6.25 μmol/g, whereas it decreased significantly to 10.04 ± 3.60
648 μmol/g in the model group ($p < 0.05$). Valeric acid contents in the mixed antibiotics group,
649 fermentation supernatant group, bacterial suspension group, and lysate supernatant group were
650 22.44 ± 5.72, 18.93 ± 3.18, 9.13 ± 4.48, and 14.39 ± 2.29 μmol/g, respectively. Among these, the
651 mixed antibiotics group and fermentation supernatant group were significantly higher than the
652 model group ($p < 0.05$), whereas the bacterial suspension and lysate supernatant groups did not
653 differ significantly from the model group.
654 Fig. 7C shows changes in isobutyric acid content. Isobutyric acid is a branched-chain short-
655 chain fatty acid that is generally associated with branched-chain amino acid metabolism and
656 protein fermentation. The results showed that isobutyric acid content in the blank control group
657 was 30.98 ± 5.38 μmol/g, whereas it increased significantly to 45.69 ± 9.74 μmol/g in the model
658 group, which was significantly higher than that in the control group ($p < 0.05$). After intervention,
659 isobutyric acid contents in the mixed antibiotics group, fermentation supernatant group, bacterial
660 suspension group, and lysate supernatant group were 38.43 ± 9.39, 36.86 ± 6.78, 37.05 ± 5.47, and
661 32.65 ± 4.33 μmol/g, respectively. Among these, the lysate supernatant group was significantly
662 lower than the model group ($p < 0.05$), whereas the other intervention groups did not differ
663 significantly from the model group.
664 Fig. 7D shows changes in isovaleric acid content. Isovaleric acid is also a branched-chain

short-chain fatty acid and is related to intestinal protein fermentation metabolism. The results showed that isovaleric acid content in the blank control group was 178.99 ± 23.21 μmol/g, whereas it increased significantly to 368.22 ± 64.03 μmol/g in the model group, which was significantly higher than that in the control group ($p < 0.05$). After intervention, isovaleric acid contents in the mixed antibiotics group, fermentation supernatant group, bacterial suspension group, and lysate supernatant group were 241.69 ± 50.03, 203.52 ± 57.95, 185.80 ± 36.19, and 184.89 ± 51.18 μmol/g, respectively, all of which were significantly lower than that in the model group ($p < 0.05$).

3.3.3 Analysis of Gastric Mucosal Inflammatory Factors and the Virulence Factor CagA

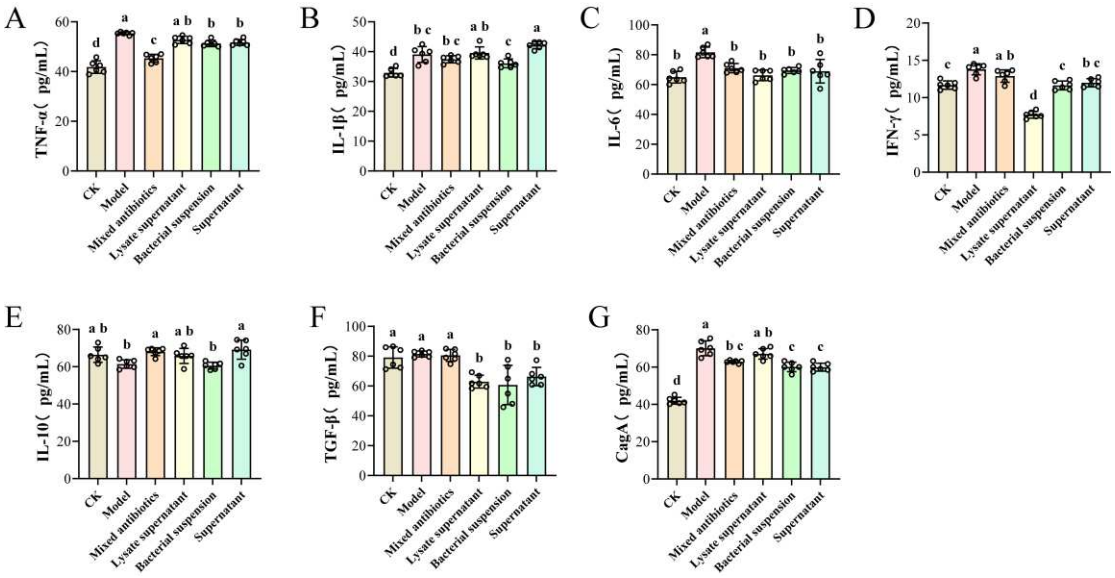


Fig. 8 Effects of different treatments on serum inflammatory factors, fibrosis-related factors, and the gastric mucosal virulence factor CagA in *H. pylori*-infected mice. A: TNF-α; B: IL-1β; C: IL-6; D: IFN-γ; E: IL-10; F: TGF-β; G: CagA.

Note: A-D represent pro-inflammatory factors, E represents an anti-inflammatory factor, F represents a fibrosis-related factor, and G represents the *H. pylori* virulence factor. Different lowercase letters indicate significant differences between groups ($p < 0.05$).

Fig. 8 shows the effects of different *B. longum* Bianquejun 19 treatments on serum inflammatory factors, fibrosis-related factors, and gastric tissue CagA levels in *H. pylori*-infected mice. TNF-α, IL-1β, IL-6, and IFN-γ are pro-inflammatory factors; IL-10 is an anti-inflammatory factor; TGF-β is related to tissue repair and fibrosis; and CagA is an important *H. pylori* virulence factor.

TNF-α (Fig. 8A) is an important pro-inflammatory factor involved in inflammatory responses. The results showed that the TNF-α level in the control group was 41.81 ± 2.52 pg/mL, whereas it increased significantly to 55.39 ± 0.56 pg/mL in the model group ($p < 0.05$). After intervention, TNF-α in the mixed antibiotics group decreased significantly to 45.35 ± 1.60 pg/mL. Levels in the bacterial suspension group, fermentation supernatant group, and lysate supernatant group were 51.31 ± 1.28, 51.74 ± 1.19, and 52.73 ± 1.47 pg/mL, respectively; among these, the bacterial suspension and fermentation supernatant groups were significantly lower than the model group ($p < 0.05$).

IL-1β (Fig. 8B) is an important pro-inflammatory factor in the inflammatory cascade. The results showed that the IL-1β level in the control group was 32.90 ± 1.44 pg/mL, whereas it increased significantly to 39.05 ± 2.64 pg/mL in the model group ($p < 0.05$). IL-1β levels in the mixed antibiotics group, lysate supernatant group, and bacterial suspension group were 37.43 ± 1.21, 39.55 ± 2.03, and 36.08 ± 1.47 pg/mL, respectively, with no significant differences compared with the model group. The fermentation supernatant group increased to 42.18 ± 1.14 pg/mL, which was significantly higher than the model group ($p < 0.05$).

IL-6 (Fig. 8C) is a pro-inflammatory factor involved in inflammatory responses and tissue injury. The results showed that the IL-6 level in the control group was 64.97 ± 3.94 pg/mL,

whereas it increased significantly to 81.59 ± 3.53 pg/mL in the model group ($p < 0.05$). After intervention, IL-6 levels in the mixed antibiotics group, lysate supernatant group, bacterial suspension group, and fermentation supernatant group were 71.05 ± 3.09, 66.21 ± 3.57, 69.45 ± 1.98, and 68.93 ± 7.91 pg/mL, respectively, all of which were significantly lower than that in the model group ($p < 0.05$).

IFN-γ (Fig. 8D) is a pro-inflammatory factor associated with Th1-type immune responses. The results showed that the IFN-γ level in the control group was 11.69 ± 0.56 pg/mL, whereas it increased significantly to 13.79 ± 0.74 pg/mL in the model group ($p < 0.05$). The IFN-γ level in the mixed antibiotics group was 12.89 ± 0.83 pg/mL, with no significant difference compared with the model group. Levels in the fermentation supernatant group, lysate supernatant group, and bacterial suspension group were 11.99 ± 0.61, 7.70 ± 0.47, and 11.64 ± 0.59 pg/mL, respectively, all of which were significantly lower than that in the model group ($p < 0.05$).

IL-10 (Fig. 8E) is an important anti-inflammatory factor that participates in negative regulation of inflammatory responses. The results showed that the IL-10 level in the control group was 66.46 ± 4.09 pg/mL and decreased to 61.47 ± 2.26 pg/mL in the model group. After intervention, IL-10 increased significantly to 68.04 ± 2.11 pg/mL in the mixed antibiotics group and to 69.16 ± 5.12 pg/mL in the fermentation supernatant group ($p < 0.05$). Levels in the lysate supernatant group and bacterial suspension group were 65.80 ± 4.06 and 60.58 ± 1.86 pg/mL, respectively, with no significant differences compared with the model group.

TGF-β (Fig. 8F) is an important factor involved in inflammatory regulation and tissue repair. The TGF-β level was 79.11 ± 7.17 pg/mL in the control group and 81.45 ± 1.97 pg/mL in the model group. The level in the combined antibiotic group was 80.52 ± 4.01 pg/mL, which was not

significantly different from that in the model group. In contrast, the levels in the lysate supernatant, bacterial suspension, and fermentation supernatant groups were 62.91 ± 4.27, 60.68 ± 13.17, and 66.29 ± 6.14 pg/mL, respectively, all of which were significantly lower than that in the model group ($p < 0.05$).

CagA (Fig. 8G) is an important virulence factor of *H. pylori* and is closely associated with host-cell injury and inflammatory responses. The CagA level was 41.97 ± 1.86 pg/mL in the control group and increased significantly to 70.08 ± 3.99 pg/mL in the model group ($p < 0.05$). Following intervention, the CagA levels in the combined antibiotic, bacterial suspension, and fermentation supernatant groups were 62.87 ± 0.73, 60.08 ± 2.54, and 59.99 ± 2.12 pg/mL, respectively, all of which were significantly lower than that in the model group ($p < 0.05$). The CagA level in the lysate supernatant group was 67.11 ± 2.80 pg/mL and did not differ significantly from that in the model group.

4 Discussion

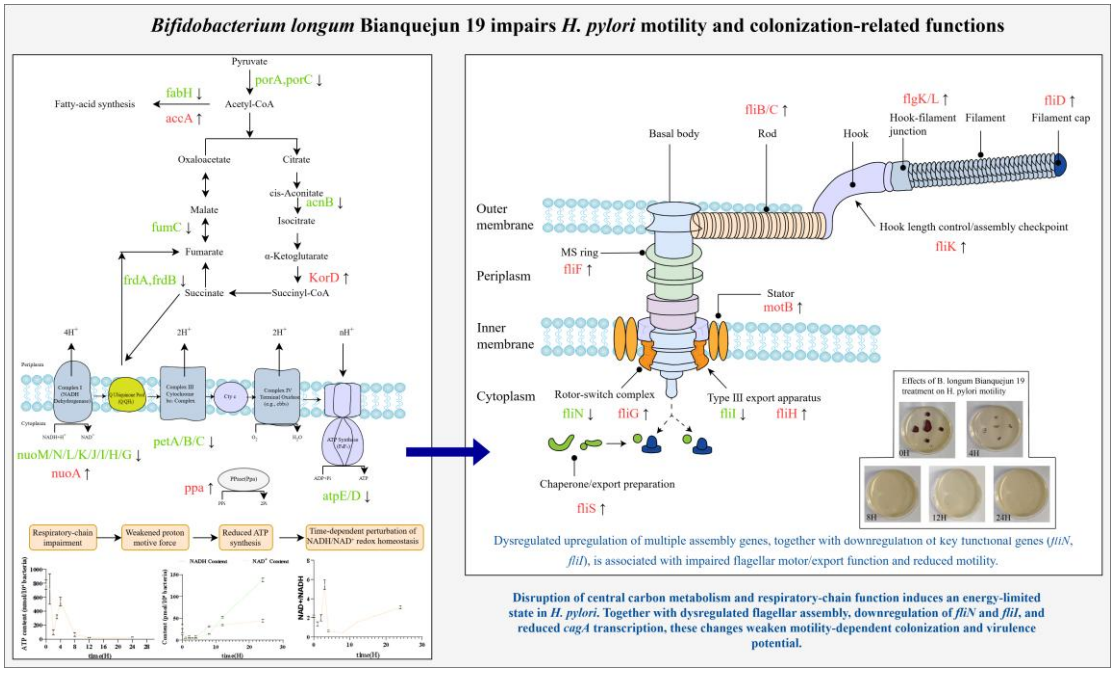


Fig. 9 Proposed model linking disruption of energy metabolism to impaired flagellar motility and colonization-

related functions in *H. pylori* following treatment with *B. longum* Bianquejun 19.

The results shown in Fig. 1 demonstrated that the different preparations of *B. longum* Bianquejun 19 inhibited *H. pylori* growth to varying degrees and reduced its adhesion to and invasion-associated signals in GES-1 gastric epithelial cells. The fermentation supernatant exhibited the strongest antibacterial activity and retained substantial inhibitory activity after pH neutralization, indicating that its effect could not be attributed entirely to acidification. The fermentation products may therefore contain other soluble antibacterial components,but is mediated by soluble non-acidic bioactive components[25]. The bacterial suspension showed a marked effect in the competition mode, suggesting that viable bacteria may interfere with contact between *H. pylori* and epithelial cells by occupying adhesion sites or modifying the local microenvironment. The relatively strong effects of the fermentation and lysate supernatants in some exclusion or displacement modes further suggest that extracellular metabolites and bacterial cell-derived bioactive components may jointly interfere with the early stages of colonization[12][15][26].

On this basis, Figures 2 and 3 further demonstrated that *B. longum* Bianquejun 19 disrupted the energy-metabolic basis of *H. pylori* [27]. Downregulation of the central carbon metabolism-related genes frdA, frdB, fumC, acnB, porA, and porC, together with the initial increase and subsequent decrease in acetyl-CoA levels, suggests disturbances in pyruvate input into acetyl-CoA metabolism, noncanonical tricarboxylic acid metabolic branches, and carbon-flow distribution[9][28]. Downregulation of petA, petB, petC, and most nuo family genes indicates that respiratory-chain electron transfer and proton translocation may have been impaired[29]. The downregulation of atpE and atpD, together with the sustained decrease in ATP levels, further

762 supports the conclusion that the bacteria entered an energy-limited state. The upregulation of nuoA
763 and ppa may reflect localized compensatory responses that were insufficient to offset the overall
764 functional impairment caused by the simultaneous downregulation of multiple key subunits. The
765 time-dependent fluctuations in NADH, NAD^+, and the NAD^+/NADH ratio indicate persistent
766 disruption of redox homeostasis rather than a simple unidirectional change[8][30].

767 Fig. 4 showed that most genes associated with flagellar structure, assembly, and motor
768 function were upregulated in *H. pylori*, which may represent a compensatory response aimed at
769 maintaining flagellar structure under stress conditions. However, fliN and fliI were significantly
770 downregulated[31]. fliN encodes an important component of the rotor-switch complex[32], whereas
771 fliI encodes the ATPase of the flagellar export system[33]. When considered together with the
772 marked decrease in ATP levels, these findings suggest that, despite compensatory activation of
773 some structural genes, the bacteria were unable to maintain normal protein export, motor
774 regulation, and flagellar assembly. The marked reduction in the motility halo and its disappearance
775 after 8 h in the soft-agar assay, together with bacterial deformation, reduced flagellar numbers,
776 flagellar breakage, and flagellar detachment observed by transmission electron microscopy, further
777 confirmed impairment of the motility system at both functional and morphological levels[6][7].
778 Notably, cagA transcript abundance decreased from 17,760.56 to 8,309.02 TPM, representing a
779 reduction of 53.22%. This finding suggests that *B. longum* Bianquejun 19 also reduced CagA-
780 associated virulence potential. The direction of this change was consistent with the reduction in
781 gastric tissue CagA protein levels observed in some intervention groups in the animal experiment.

782 Based on the above results of transcriptome analysis, metabolite detection, motility assays
783 and ultrastructural observation, this study established a proposed mode of action for *B. longum*

784 Bianquejun 19 against *H. pylori* (Fig. 9). Following treatment with *B. longum* Bianquejun 19,
785 central carbon metabolism-related genes including frdA, frdB, fumC, acnB, porA and porC were
786 downregulated, accompanied by dynamic alterations in acetyl-CoA levels, indicating disruptions
787 to pyruvate influx into acetyl-CoA, the non-canonical tricarboxylic acid (TCA) metabolic shunt,
788 and carbon flux distribution. Meanwhile, petA, petB, petC and most nuo family genes were
789 downregulated, along with reduced expression of atpE and atpD, continuous declines in ATP
790 content and fluctuating NADH/NAD^+ homeostasis. These findings demonstrate impaired
791 functions of respiratory chain electron transport, proton translocation and ATP synthesis, rendering
792 the bacteria energy-limited. On this basis, although partial flagellar structural and assembly-related
793 genes exhibited compensatory upregulation, the flagellar rotor-switch complex gene fliN and the
794 flagellar export ATPase gene fliI were markedly downregulated. Coupled with insufficient ATP
795 supply, this may restrict flagellar protein export, motor regulation and structural maintenance. In
796 soft agar assays, the swimming halo was drastically reduced and vanished after 8 hours.
797 Transmission electron microscopy revealed bacterial morphological deformation, fewer flagella,
798 flagellar breakage or detachment from bacterial cells, further corroborating impaired flagellar
799 motility systems at both functional and morphological levels. In addition, the transcriptional
800 abundance of cagA decreased by 53.22%, suggesting attenuated CagA-associated virulence
801 potential. Collectively, energy metabolic imbalance and flagellar dysfunction induced by *B.*
802 *longum* Bianquejun 19 are interrelated, jointly weakening the motility, motility-dependent
803 colonization capacity and persistent pathogenic potential of *H. pylori*.
804 Fig. 6 demonstrated at the animal level that *H. pylori* infection induced gastric epithelial
805 injury, disorganization of gastric glands, increased inflammatory-cell infiltration, and elevated

collagen deposition in mice. Intervention with the different *B. longum* Bianquejun 19 preparations reduced both the inflammatory infiltration area and collagen-positive area to varying degrees, indicating that *B. longum* Bianquejun 19 helped alleviate infection-associated gastric mucosal injury and improve tissue remodeling. In combination with the in vitro findings, this protective effect may be associated with the suppression of bacterial growth, adhesion and invasion, energy metabolism, motility, and virulence potential.

Fig. 7 shows that acetic acid and valeric acid decrease while isobutyric acid and isovaleric acid increase after H. pylori infection, indicating that the infectious state is accompanied by alterations in the colonic metabolic environment[34]. Changes in short-chain fatty acids may also be associated with intestinal metabolism and inflammatory status[35]. The effects of the different *B. longum* Bianquejun 19 preparations on short-chain fatty acids were preparation-dependent. The fermentation supernatant primarily promoted the recovery of acetate and valerate, the lysate supernatant produced a more pronounced reduction in isobutyrate, and all probiotic intervention groups reduced isovalerate levels. Fig. 8 further showed that IL-6 levels decreased in all probiotic intervention groups, whereas TNF-α, IFN-γ, TGF-β, and IL-10 exhibited group-dependent changes. IL-1β did not show a consistent decrease. Gastric tissue CagA levels were significantly reduced in the bacterial suspension and fermentation supernatant groups. Together with the in vitro downregulation of cagA transcription, these findings support the suppression of virulence-related phenotypes[36].

Taken together, the results presented in Figures 1–8 indicate that *B. longum* Bianquejun 19 interfered with *H. pylori* through multiple levels of action. It initially inhibited bacterial growth and reduced adhesion to and invasion of gastric epithelial cells. It subsequently disrupted central

carbon metabolism, respiratory-chain function, ATP synthesis, and NADH/NAD^+ homeostasis, placing the bacteria in an energy-limited state. On this basis, flagellar export, motor regulation, and structural integrity were impaired, resulting in reduced motility and colonization-related functions. These changes were accompanied by decreased cagA transcription and reduced gastric tissue CagA levels in some animal intervention groups. Collectively, these alterations indicate weakening of motility-dependent adhesion, colonization, and persistent-infection potential in *H. pylori*. They were also accompanied by reduced gastric mucosal inflammation and collagen deposition and by improvement of the colonic short-chain fatty acid profile, together constituting the overall effects of *B. longum* Bianquejun 19 on colonization-associated pathogenic processes of *H. pylori*.

This study has several limitations. First, the gastric *H. pylori* burden was not directly quantified in the animal experiment. Therefore, a reduction in in vivo colonization requires further verification through culture-based enumeration, quantitative PCR, or in situ detection. Second, the cagA transcription data and gastric tissue CagA protein data were obtained from an in vitro co-culture system and an animal model, respectively. Although the results showed changes in the same direction, they do not establish a direct causal relationship. Moreover, the efficiency of CagA translocation through the type IV secretion system was not directly measured. Finally, changes in short-chain fatty acids cannot substitute for evidence regarding microbial community structure and function. Future studies should combine 16S rRNA gene sequencing or metagenomic sequencing with intervention-blocking experiments to further clarify the contribution of intestinal metabolic changes to gastric mucosal protection.

5 Conclusions

This study systematically evaluated the effects of the probiotic *B. longum* Bianquejun 19 on *H. pylori* growth, adhesion and invasion, energy metabolism, motility, virulence-related phenotypes, and *H. pylori*-induced gastric mucosal inflammatory injury. The results demonstrated that the different *B. longum* Bianquejun 19 preparations inhibited *H. pylori* growth to varying degrees and reduced its adhesion to and invasion of GES-1 gastric epithelial cells. The fermentation supernatant exhibited strong direct antibacterial activity, whereas the bacterial suspension and lysate supernatant interfered with early colonization-related processes under different intervention modes.

Transcriptomic and metabolite measurements showed that *B. longum* Bianquejun 19 disrupted central carbon metabolism, acetyl-CoA homeostasis, respiratory-chain function, ATP synthesis, and NADH/NAD^+ redox balance in *H. pylori*. Significant changes occurred in multiple genes associated with central carbon metabolism, respiratory-chain complexes, and ATP synthase, together with dynamic alterations in acetyl-CoA, ATP, NADH, and NAD^+ levels. These findings indicate that *H. pylori* entered a pronounced energy-limited and redox-imbalanced state following treatment.

Analyses of flagellar gene expression, soft-agar motility, and transmission electron microscopy further demonstrated that *B. longum* Bianquejun 19 impaired flagellar structure and motility in *H. pylori*. Although several genes involved in flagellar structure and assembly were compensatorily upregulated, the key functional genes fliN and fliI were downregulated. The motility halo was markedly reduced or completely absent, and bacterial deformation, reduced flagellar numbers, and flagellar breakage were observed. In addition, cagA transcript abundance

decreased by 53.22%, suggesting reduced CagA-associated virulence potential.

The in vivo results showed that *H. pylori* infection induced gastric epithelial injury, inflammatory-cell infiltration, collagen deposition, and abnormal serum inflammatory mediator levels in mice. These changes were accompanied by increased gastric tissue CagA levels and alterations in the colonic short-chain fatty acid profile. Following intervention with the different *B. longum* Bianquejun 19 preparations, gastric inflammatory infiltration and collagen deposition were alleviated to varying degrees. Some pro-inflammatory factors and TGF-β levels decreased, IL-10 increased in some treatment groups, gastric tissue CagA levels decreased in the bacterial suspension and fermentation supernatant groups, and the short-chain fatty acid profile showed preparation-dependent improvement.

In conclusion, *B. longum* Bianquejun 19 inhibited *H. pylori* growth and its adhesion to and invasion of gastric epithelial cells and disrupted central carbon metabolism, respiratory-chain function, ATP synthesis, and NADH/NAD^+ redox homeostasis, thereby placing the bacteria in an energy-limited state. At the same time, impairment of flagellar export, motor regulation, and structural integrity reduced bacterial motility and motility-dependent colonization-related functions and was accompanied by decreased cagA transcription and reduced gastric tissue CagA levels in some intervention groups. Collectively, these effects weakened the colonization and persistent pathogenic potential of *H. pylori* and were accompanied by alleviation of gastric mucosal inflammation and improvement of the colonic short-chain fatty acid profile. This study provides experimental evidence supporting the development of *B. longum* Bianquejun 19 as an adjunctive intervention strain against *H. pylori* infection and as a source of bioactive metabolites.

Conflicts of Interest Statement

There are no conflicts to declare.

Author contributions

Yajie Zhang (First Author): Conceptualization, Data Curation, Formal Analysis, Investigation, Methodology, Software, Visualization, Writing – Original Draft, Writing – Review & Editing.

Lijuan Kang: Resources, Investigation.

Yinqing Li: Resources, Investigation.

Liang Zhao: Methodology, Software, Formal Analysis.

Yuanhong Xie: Methodology, Validation.

Hongxing Zhang: Methodology, Validation.

Ran Wang(Corresponding Author): Conceptualization, Funding Acquisition, Supervision, Writing – Review & Editing.

Junhua Jin (Corresponding Author): Conceptualization, Project Administration, Supervision, Writing – Review & Editing.

All authors have read and agreed to the published version of the manuscript.

Data availability

The data that support the findings of this study are available from the corresponding author upon reasonable request.

Funding Declaration

This research did not receive any specific grant from funding agencies in the public, commercial, or not-for-profit sectors.

References

[1]Amieva, M., & Peek, R. M., Jr. (2016). Pathobiology of *Helicobacter pylori*–Induced Gastric Cancer. *Gastroenterology, 150*(1), 64–78. https://doi.org/10.1053/j.gastro.2015.09.004.

[2]Yang, H., & Hu, B. (2022). Immunological Perspective: *Helicobacter pylori* Infection and Gastritis. *Mediators of Inflammation, 2022*, 1–11. https://doi.org/10.1155/2022/2944156.

[3]Abdullah, M., Greenfield, L. K., Bronte-Tinkew, D., Capurro, M. I., Rizzuti, D., & Jones, N. L. (2019). VacA promotes CagA accumulation in gastric epithelial cells during *Helicobacter pylori* infection. *Scientific Reports, 9*(1). https://doi.org/10.1038/s41598-018-37095-4.

[4]Amieva, M. R., Vogelmann, R., Covacci, A., Tompkins, L. S., Nelson, W. J., & Falkow, S. (2003). Disruption of the Epithelial Apical-Junctional Complex by *Helicobacter pylori* CagA. *Science, 300*(5624), 1430–1434. https://doi.org/10.1126/science.1081919.

[5]Odenbreit, S., Püls, J., Sedlmaier, B., Gerland, E., Fischer, W., & Haas, R. (2000). Translocation of *Helicobacter pylori* CagA into Gastric Epithelial Cells by Type IV Secretion. *Science, 287*(5457), 1497–1500. https://doi.org/10.1126/science.287.5457.1497.

[6]Gu, H. (2017). Role of Flagella in the Pathogenesis of *Helicobacter pylori. Current Microbiology, 74*(7), 863–869. https://doi.org/10.1007/s00284-017-1256-4.

[7]Ottemann, K. M., & Lowenthal, A. C. (2002). *Helicobacter pylori* Uses Motility for Initial Colonization and To Attain Robust Infection. *Infection and Immunity, 70*(4), 1984–1990. https://doi.org/10.1128/iai.70.4.1984-1990.2002.

[8]Chen, M., Andersen, L. P., Zhai, L., & Kharazmi, A. (1999). Characterization of the respiratory chain of *Helicobacter pylori*. *FEMS Immunology & Medical Microbiology, 24*(2), 169–174. https://doi.org/10.1111/j.1574-695x.1999.tb01278.x.

939 [9]Marais, A., Mendz, G. L., Hazell, S. L., & Mégraud, F. (1999). Metabolism and Genetics of
940 *Helicobacter pylori* : the Genome Era. *Microbiology and Molecular Biology Reviews, 63*(3),
941 642–674. https://doi.org/10.1128/mmbr.63.3.642-674.1999.
942 [10]Malfertheiner, P., Megraud, F., Rokkas, T., Gisbert, J. P., Liou, J.-M., Schulz, C., Gasbarrini,
943 A., Hunt, R. H., Leja, M., O’ Morain, C., Rugge, M., Suerbaum, S., Tilg, H., Sugano, K., & El-
944 Omar, E. M. (2022). Management of *Helicobacter pylori* infection: the Maastricht VI/Florence
945 consensus report. *Gut, 71*(9), 1724–1762. https://doi.org/10.1136/gutjnl-2022-327745.
946 [11]Yang, Z., Zhou, Y., Han, Z., He, K., Zhang, Y., Wu, D., & Chen, H. (2024). The effects of
947 probiotics supplementation on *Helicobacter pylori* standard treatment: an umbrella review of
948 systematic reviews with meta-analyses. *Scientific Reports, 14*(1). https://doi.org/10.1038/s41598-
949 024-59399-4.
950 [12]Chenoll, E., Casinos, B., Bataller, E., Astals, P., Echevarría, J., Iglesias, J. R., Balbarie, P.,
951 Ramón, D., & Genovés, S. (2011). Novel Probiotic *Bifidobacterium bifidum* CECT 7366 Strain
952 Active against the Pathogenic Bacterium *Helicobacter pylori*. *Applied and Environmental*
953 *Microbiology, 77*(4), 1335–1343. https://doi.org/10.1128/aem.01820-10.
954 [13]Collado, M. C., González, A., González, R., Hernández, M., Ferrús, M. A., & Sanz, Y. (2005).
955 Antimicrobial peptides are among the antagonistic metabolites produced by *Bifidobacterium*
956 against *Helicobacter pylori*. *International Journal of Antimicrobial Agents, 25*(5), 385–391.
957 https://doi.org/10.1016/j.ijantimicag.2005.01.017.
958 [14]Sgouras, D., Maragkoudakis, P., Petraki, K., Martinez-Gonzalez, B., Eriotou, E.,
959 Michopoulos, S., Kalantzopoulos, G., Tsakalidou, E., & Mentis, A. (2004). In Vitro and In Vivo
960 Inhibition of *Helicobacter pylori* by *Lactobacillus casei* Strain Shirota. *Applied and*

961 *Environmental Microbiology, 70*(1), 518–526. https://doi.org/10.1128/aem.70.1.518-526.2004.

962 [15]de Klerk, N., Maudsdotter, L., Gebreegziabher, H., Saroj, S. D., Eriksson, B., Eriksson, O. S.,

963 Roos, S., Lindén, S., Sjölinder, H., & Jonsson, A.-B. (2016). *Lactobacilli* Reduce *Helicobacter*

964 *pylori* Attachment to Host Gastric Epithelial Cells by Inhibiting Adhesion Gene Expression.

965 *Infection and Immunity, 84*(5), 1526–1535. https://doi.org/10.1128/iai.00163-16.

966 [16]Kwok, T., Backert, S., Schwarz, H., Berger, J., & Meyer, T. F. (2002). Specific Entry of

967 *Helicobacter pylori* into Cultured Gastric Epithelial Cells via a Zipper-Like Mechanism. *Infection*

968 *and Immunity, 70*(4), 2108–2120. https://doi.org/10.1128/iai.70.4.2108-2120.2002.

969 [17]Chen, S., Zhou, Y., Chen, Y., & Gu, J. (2018). fastp: an ultra-fast all-in-one FASTQ

970 preprocessor. *Bioinformatics, 34*(17), i884–i890. https://doi.org/10.1093/bioinformatics/bty560.

971 [18]Zhao, Jianhua, Linmeng Liu, Jichen Han, et al. Majorbio Cloud 2026 Provides

972 Comprehensive Analysis Workflows for Microbiome[J]. *iMeta*, 2026, e70109.

973 https://doi.org/10.1002/imt2.70109.

974 [19]Li, D., Liu, C.-M., Luo, R., Sadakane, K., & Lam, T.-W. (2014). MEGAHIT: An ultra-fast

975 single-node solution for large and complex metagenomics assembly via succinct de Bruijn graph

976 (Version 2). arXiv. https://doi.org/10.48550/ARXIV.1409.7208 .

977 [20]Hyatt, D., Chen, G.-L., LoCascio, P. F., Land, M. L., Larimer, F. W., & Hauser, L. J. (2010).

978 Prodigal: prokaryotic gene recognition and translation initiation site identification. *BMC*

979 *Bioinformatics, 11*(1). https://doi.org/10.1186/1471-2105-11-119.

980 [21]Buchfink, B., Xie, C., & Huson, D. H. (2014). Fast and sensitive protein alignment using

981 DIAMOND. *Nature Methods, 12*(1), 59–60. https://doi.org/10.1038/nmeth.3176.

982 [22]Lee, A., O’Rourke, J., De Ungria, M., Robertson, B., Daskalopoulos, G., & Dixon, M.

983 (1997). A standardized mouse model of *Helicobacter pylori* infection: Introducing the Sydney
984 strain. *Gastroenterology, 112*(4), 1386 – 1397. https://doi.org/10.1016/s0016-5085(97)70155-0.
985 [23]Schneider, C. A., Rasband, W. S., & Eliceiri, K. W. (2012). NIH Image to ImageJ: 25 years of
986 image analysis. *Nature Methods, 9*(7), 671 – 675. https://doi.org/10.1038/nmeth.2089.
987 [24]Zhao, G., Nyman, M., & Ake Jönsson, J. (2006). Rapid determination of short - chain fatty
988 acids in colonic contents and faeces of humans and rats by acidified water - extraction and
989 direct - injection gas chromatography. *Biomedical Chromatography, 20*(8), 674 – 682.
990 https://doi.org/10.1002/bmc.580.
991 [25]Sornsenee, P., Surachat, K., Wong, T., Kaewdech, A., Saki, M., & Romyasamit, C. (2024).
992 Lyophilized cell-free supernatants of *Limosilactobacillus* fermentum T0701 exhibited antibacterial
993 activity against *Helicobacter pylori*. *Scientific Reports, 14*(1), 14352.
994 https://doi.org/10.1038/s41598-024-64443-4.
995 [26]Zuo, F., Somiah, T., Gebremariam, H. G., & Jonsson, A.-B. (2022). Lactobacilli Downregulate
996 Transcription Factors in *Helicobacter pylori* That Affect Motility, Acid Tolerance and
997 Antimicrobial Peptide Survival. *International Journal of Molecular Sciences, 23*(24), 15451.
998 https://doi.org/10.3390/ijms232415451.
999 [27]Han, B., Zhang, Z., Xie, Y., Hu, X., Wang, H., Xia, W., Wang, Y., Li, H., Wang, Y., & Sun, H.
1000 (2018). Multi-omics and temporal dynamics profiling reveal disruption of central metabolism in
1001 *Helicobacter pylorion* bismuth treatment. Chemical Science, 9(38), 7488–7497.
1002 https://doi.org/10.1039/c8sc01668b.
1003 [28]Hughes, N. J., Clayton, C. L., Chalk, P. A., & Kelly, D. J. (1998). *Helicobacter pylori*
1004 porCDAB and oorDABC Genes Encode Distinct Pyruvate:Flavodoxin and 2-

1005 Oxoglutarate:Acceptor Oxidoreductases Which Mediate Electron Transport to NADP. *Journal of*
1006 *Bacteriology, 180*(5), 1119 – 1128. https://doi.org/10.1128/jb.180.5.1119-1128.1998.
1007 [29]Yao, X., Xiao, S., & Zhou, L. (2021). Integrative proteomic and metabolomic analyses reveal
1008 the mechanism by which bismuth enables *Helicobacter pylori* eradication. *Helicobacter, 26*(6),
1009 e12846. https://doi.org/10.1111/hel.12846.
1010 [30]Van Amsterdam, K., & Van Der Ende, A. (2004). *Helicobacter pylori* HP1034 (ylxH) is
1011 required for motility. *Helicobacter, 9*(5), 387 – 395. https://doi.org/10.1111/j.1083-
1012 4389.2004.00268.x.
1013 [31]Suerbaum, S., Coombs, N., Patel, L., Pscheniza, D., Rox, K., Falk, C., Gruber, A. D.,
1014 Kershaw, O., Chhatwal, P., Brönstrup, M., Bilitewski, U., & Josenhans, C. (2022). Identification
1015 of Antimotilins, Novel Inhibitors of *Helicobacter pylori* Flagellar Motility That Inhibit Stomach
1016 Colonization in a Mouse Model. *mBio, 13*(2), e03755-21. https://doi.org/10.1128/mbio.03755-21.
1017 [32]Lowenthal, A. C., Hill, M., Sycuro, L. K., Mehmood, K., Salama, N. R., & Ottemann, K. M.
1018 (2009). Functional Analysis of the *Helicobacter pylori* Flagellar Switch Proteins. *Journal of*
1019 *Bacteriology, 191*(23), 7147 – 7156. https://doi.org/10.1128/jb.00749-09.
1020 [33]Jenks, P. J., Foynes, S., Ward, S. J., Constantinidou, C., Penn, C. W., & Wren, B. W. (1997). A
1021 flagellar-specific ATPase (FliI) is necessary for flagellar export in *Helicobacter pylori. FEMS*
1022 *Microbiology Letters, 152*(2), 205 – 11. https://doi.org/10.1111/j.1574-6968.1997.tb10429.x.
1023 [34]Kienesberger, S., Cox, L. M., Livanos, A., Zhang, X.-S., Chung, J., Perez-Perez, G. I.,
1024 Gorkiewicz, G., Zechner, E. L., & Blaser, M. J. (2016). Gastric *Helicobacter pylori* Infection
1025 Affects Local and Distant Microbial Populations and Host Responses. *Cell Reports, 14*(6), 1395 –
1026 1407. https://doi.org/10.1016/j.celrep.2016.01.017.

[35]Huang, Y., Ding, Y., Xu, H., Shen, C., Chen, X., & Li, C. (2021). Effects of sodium butyrate supplementation on inflammation, gut microbiota, and short‐chain fatty acids in *Helicobacter pylori*‐infected mice. *Helicobacter, 26*(2). https://doi.org/10.1111/hel.12785.

[36]Sharndama, H. C., & Mba, I. E. (2022). *Helicobacter pylori*: an up-to-date overview on the virulence and pathogenesis mechanisms. *Brazilian Journal of Microbiology, 53*(1), 33–50. https://doi.org/10.1007/s42770-021-00675-0.